NINETEENTH EUROPEAN ROTORCRAFT FORUM

Paper $n°$ C22

# - CP-ROT -
# First Results from Pressure Instrumented BO105 Hingeless Model Rotor Tests

by

Berend G. van der Wall
Institute for Flight Mechanics, DLR Braunschweig, Germany

September 14-16, 1993
CERNOBBIO (COMO)
ITALY

ASSOCIAZIONE INDUSTRIE AEROSPAZIALI
ASSOCIAZIONE ITALIANA DI AERONAUTICA ED ASTRONAUTICA

# Abstract

CP-ROT (CP pressure coefficient measurement on the ROTating blade) is a common project of several institutes of DLR. Its purpose is to get insight into rotor aeromechanics and unsteady aerodynamics via measurement of the pressure distribution on the upper and lower rotor blade surface. Additionally, the blade bending moment distribution is measured via strain gages along the radius in flap, lead-lag and torsion. In December 1992 a highly instrumented model rotor (40% scaled BO105 hingeless rotor system, rectangular blades, NACA 23012 mod. airfoil) was tested in the German-Dutch Windtunnel (DNW) within the BRITE/EURAM project HELINOISE [1]. The rotor was equipped with 124 absolute pressure sensors and 32 strain gages (all on one blade) for high frequency measurement of the surface pressures and blade deformations. A specially made data acquisition system allowed the simultaneous measurement of all these sensors with a sampling rate of about 36kHz (2048 samples per revolution). The data match the analyses requirements of unsteady aerodynamics and aeroacoustics as well. With this equipment, the pressure distribution along the leading edge of the blade (3% chord on upper and lower side) at radial positions from 60% up to 99% and at three radial positions along chord ($x = 0.75, 0.87$ and $0.97$) could be evaluated experimentally. (This instrumentation corresponds to CP-ROT phase I; an even larger number of pressure sensors is planned in future phases of CP-ROT.) The test matrix included hover as well as forward flight configurations up to advance ratios of $\mu = 0.352$. Of special interest were a large number of blade-vortex interaction (BVI) cases in the range of $\mu = 0.089$ to $\mu = 0.314$.

This paper investigates a low speed BVI case at $\mu = 0.149$ with a shaft angle of $\alpha_S = +5.05^\circ$ (tilted backwards) at a thrust coefficient of $C_T/\sigma = 0.058$, representing a $6^\circ$ descent flight condition. Also, a high speed BVI case at $\mu = 0.314$, $\alpha_S = -0.94$ and $C_T/\sigma$ as before is investigated. With the low speed configuration, two tests were conducted on different days in order to evaluate the repeateability which was found to be excellent. From the time history of the leading edge pressure sensors, the BVI locations can be clearly identified. The vortex core radii can also be identified to first order accuracy from these signals. The aerodynamic lift at three radial positions is related direcly to the leading edge pressure while the aerodynamic moment is found to act with a small time delay.

The BVI effects at the high speed case are also interesting. The vortex pattern shows pairs of votices on the advancing side, rotating in opposite directions. An investigation of the aerodynamic lift distribution shows negative lift on the outer 20% of the blade from $\psi = 85^\circ$ to $175^\circ$. Thus, at the tip a vortex of negative circulation is created and more inboard, a vortex of positive circulation is forming because of another significant radial gradient in the blade's circulation.

The vortex core radii found in the high speed case correlate well to those found at the low speed and a core radius widening formula was extracted. The results show that the core radius grows about 20% chord per $300^\circ$ azimuthal vortex age and the core radii of the "youngest" vortices found is in the range of 20% chord. This is a commonly used value in rotor simulation codes. The associated reduced frequencies, $k$, are in the range between 1.8 and 3.4. Thus, for simulation purposes quasisteady aerodynamic theory is not applicable for correct aerodynamic loading calculations during BVI.

Due to the reproduction technique, the originally colored graphs on Fig. 2, 6, 7, 9, 12, 13 are printed only in black/white[1]


# Nomenclature

| | | | |
|---|---|---|---|
| a | pitch axis location wrt. mid-chord, pos. aft, in halfchords | $q = \rho V^2/2$ | local dynamic pressure $[N/m^2]$ |
| $c$ | airfoil chord [m] | $r, R$ | radial coordinate, radius $[m]$ |
| $C_l = L/(qc)$ | section lift coefficient | $r_c$ | vortex core radius $[m]$ |
| $C_m = M/(qc^2)$ | section moment coefficient | $t$ | time $[s]$ |
| $C_T = T/(\rho\pi R^2 V_t^2)$ | thrust coefficient | $T$ | rotor thrust $[N]$ |
| $k_t = c/(2R)$ | reduced frequency of blade tip in hover | $V = V_t(x + \mu\sin\psi)$ | local velocity $[m/s]$ |
| $k = k_t V_t/V$ | local reduced frequency | $V_t = \Omega R$ | tip speed in hover $[m/s]$ |
| $L$ | section lift $[N/m]$ | $V_T$ | wind tunnel velocity $[m/s]$ |
| $M$ | section moment $[Nm/m]$ | $x = r/R$ | radial coordinate |
| $P_u, P_l$ | air pressure on upper and lower side of the airfoil $[N/m^2]$ | $z_u, z_l$ | airfoil vertical coordinate of upper and lower side $[m]$ |

[1]The colored originals are available on request from the author in limited number.

| | | | |
|---|---|---|---|
| $\alpha_S$ | shaft angle of attack | $\mu = V_T \cos\alpha_S / V_t$ | advance ratio |
| $\beta$ | angle between vortex axis and blade leading edge | $\rho$ | air density $[kg/m^3]$ |
| $\psi = \Omega t, \psi_{BVI}$ | rotor azimuth, azimuth of a BVI event | $\Omega$ | rotor rotational speed $[rad/s]$ |
| $\Delta\psi$ | peak-to-peak azimuthal distance of a BVI event | | |

# 1 Introduction

A lot of rotor testing has been done in the past but only a few tests have been conducted with instrumented model rotor blades for high frequency pressure signals [2, 3, 4]. This is due to the complexity of the experimental setup and to the limitations of the data acquisition system. To achieve good insight into rotor unsteady aerodynamics, a lot of pressure sensors have to be installed on one blade. Additionally, the data measurement rate must be high to get also acoustically relevant pressure fluctuations and all sensor signals have to be recorded simultaneously. This is especially true when the blades are elastic and can be expected to behave slightly different during each revolution. Therefore, the decision was made in the HELINOISE program [1] to have one blade highly instrumented with all 124 pressure sensors and, in addition, with all 32 strain gages mounted in flap, lead-lag and torsional directions. All of the sensor signals were stored simultaneously for 60 revolutions at a rate of 2048 data points per revolution [5]. For data analysis, one single revolution time history and the average of all 60 cycles were stored after postprocessing. The objective was to analyse the BVI locations, the BVI impact on aerodynamic lift and moment behaviour during BVI, and to compute the blade response from the strain gage signals. In addition to the rotor instrumentation, the HELINOISE program used a microphone rig below the rotor to analyse the noise radiation. Noise results are presented in [6]. This paper, however, is confined to the aerodynamic analysis of the pressure data.

# 2 Methodology of Analyses

## 2.1 Identifying BVI Events

To analyse BVI effects most clearly, a very sensitive position of the blades must be selected. This is the leading edge of the airfoil because the pressure gradients are very large due to the highspeed flow around the airfoil nose radius. Thus, the time history of the sensors at 3% chord (upper side of the airfoil) gives the best information about the airflow the airfoil is entering. For the low speed test case the time histories at radial positions from $x = 0.6$, 0.7, 0.75, 0.8, 0.87, 0.9, 0.94, 0.97 and 0.99 are given in Fig. 1. The more inboard sections on the advancing side show BVI pressure peaks are stronger than on the retreating side. Since the Mach numbers are relatively small on both sides, this means the vortices are either closer to the airfoil on the advancing side or they are stronger in circulation. At the outer positions the retreating side BVI appears to be much stronger. This effect is mostly due to the larger Mach numbers on the advancing side where the airfoil is operating with a small supersonic regime on the upper surface.

From each of the time histories, the azimuthal and radial position of BVI can be identified as follows, assuming a positive sense of rotation of the vortices encountered. First, from Fig. 1 it can be seen that the BVI induced pressure signals are of high frequency nature (they extend only over a small azimuthal range) while the total signal has a large low frequency content (one to three harmonics) in addition. Thus, it eases the further analyses, when subtracting the first 3 harmonics from each time history; the result is shown for the radial position $x = 0.99$ in Fig. 1 below. Also, the same filtering procedure is applied to the average signal obtained from 60 revolutions and plotted below. As can be seen, the sequence and intensity of BVI is very stable since the differences between average and single revolution are very small.

On the advancing side, the blade first encounters a downwash from the vortex. This leads to a reduction of the effective angle of attack at the airfoils' leading edge and thus increases the pressure at the sensor until the maximum of the downwash is reached. Basically, the pressure is following the compressible Bernoulli-law known from airfoil theory. When the interaction is very close, say within the vortex' core radius, then the change of downwash to upwash and with it a change to lower pressure at the sensor position happens very quickly, causing a steep opposite gradient in pressure until the maximum upwash is reached. The peaks are very sharp in contour and the peak-to-peak level is the largest in a sequence of BVI events. In cases where the vortices are farther away when interacting with the airfoil, the peak-to-peak amplitudes are smaller and the distance between the peaks is larger. This is easy to explain with the Biot-Savart law for the induced velocity field of a vortex. On the retreating side the sequence of the pressure peaks is opposite because first an upwash is encountered and

then the downwash. A very close blade-vortex encounter can be found at $x = 0.99$ and $\psi_{BVI} = 295°$. In all of the BVI events, the vortex center can be localised in the middle between the two corresponding peaks.

## 2.2 BVI Locations

With this information, a contour plot of the 10/rev filtered signals in polar coordinates directly gives the vortex patterns and the BVI intensity in the rotor plane, see Fig. 2. In addition, the BVI locations as identified from Fig. 1 are marked here. The vortex positions can beo graphically obtained by plotting the gradients of each time history (the positive ones on the advancing side and the negative ones on the retreating side). Also, in Fig. 2 the calculated BVI locations using the Beddoes' model [7] are shown together with the experimentally evaluated locations. It can be seen that in general the prediction is good but at the front of the disk the vortices actually seem to travel backwards faster than predicted. From the intensity of BVI, the areas where the vortices are passing the rotor plane can be identified to be usually where the blade is almost parallel to the vortex encountered making the noise emission very significant, known as BVI noise or blade slap.

## 2.3 Vortex Core Radius Analyses

The time history of these sensors also gives information about the vortex' core radius. Assuming the blade-vortex miss distance to be within or very close to the core radius, $r_c$, the azimuthal distance $\Delta\psi$ between the two corresponding peaks of a BVI event (see Fig. 1) is a nondimensional measure for the vortex core diameter. This is defined as the geometrical length between the maximum upwash velocity before the vortex' center and the maximum downwash behind it. From Fig. 3 (top graph), that is an enlargement of Fig. 1, one can find this distance to be $\Delta\psi = 1.9°$. This includes the convection velocity of the vortex during the interaction that can be assumed to be $\mu$. The azimuth of the BVI location is found to be $\psi_{BVI} = 295.5°$. Next, using

$$\frac{r_c}{c} \approx \frac{R}{c}\left(x + \mu \sin\psi_{BVI}\right)\frac{\Delta\psi}{2}\cos\beta = \frac{\Delta\psi}{4k}\cos\beta$$

where $\beta$ is the angle with which the vortex is interacted ($\beta = 0$ when the blade leading edge and the vortex are parallel). Note that the angle between the BVI location traces in Fig. 2 and a blades leading edge line are not identically with $\beta$ except where the interaction is parallel. This is because the vortices are moving with a certain convection velocity relative to the blade. To find $\beta$, the vortex system has to be plotted for every azimuthal position separately as is done in Fig. 4 with increments in $\psi$ of 15°. The result is as follows: at certain BVI locations the instantaneous vortex traces are plotted around this BVI location and it is clearly to be seen that there are differences between $\beta$ and the angle of the BVI location traces with the blades. The data are calculated using the experimentally identified vortex locations as input for the vortex modeling. Then, the graph below (containing the BVI locations during one revolution) is completed with the instantaneous vortex positions at various BVI locations in order to identify the angle $\beta$.

In the example mentioned before, $\beta$ can be identified to be $\approx 22°$ from Fig. 4. $\psi_{BVI}$ is the rotor azimuth of the BVI event under consideration and, in combination with $\mu$, accounts for the velocity of the vortex relative to the blade. With the ratio of radius to chord being $R/c = 16.53$ for this model rotor, the core radius of the vortex is approximately 22% chord. This is well within common assumptions about the tip vortex core radii used in rotor analysis of about 20% chord. However, it has to be kept in mind that this vortex is already 320° old and originated at $\psi \approx 245°$ from the blade that is currently at $\psi = 205°$. Thus, some diffusion effects might already be in progress, widening the originally smaller vortex core.

## 2.4 Aerodynamic Lift and Moment

Three sections at $x = 0.75, 0.87, 0.97$ were instrumented along chord to obtain the chordwise pressure distribution. The time history of these signals will show the BVI effect along chord and therefore its effect on lift and moment after proper integration. Fig. 5 shows typical pressure distributions for the 3 sections at the azimuth $\psi = 90°$ and 270° (data from the high speed case). The pressure distributions represent the raw data, averaged over 60 cycles. A lot of these signals do have a steady offset that will affect the calculation of the steady component of the aerodynamic lift and especially the moment. For a better estimation of these steady components, the various offsets have to be corrected manually which is a cumbersome job that needs some experience. It must be noted, that the dynamic part of lift and moment is not affected by this correction procedure. In Fig. 4 at $\psi = 90°$ the outer sections clearly show supersonic regions on the airfoils' upper surface. The Mach number is about 0.84 for the section at $x = 0.99$, 0.76 at $x = 0.87$ and 0.68 at $x = 0.75$. The reason that these supersonic areas are not larger is due to the relatively small angles of attack. On the retreating side, no supersonic areas are to be found and thus typical subcritical pressure distributions are present. The Mach numbers are 0.43, 0.36

and 0.28 at the radial positions $x = 0.99, 0.87, 0.75$, respectively. Large pressure peaks at the leading edge on the upper side indicate large angles of attack that are necessary to balance the rotor.

The integration of the pressure is done at every data point during the revolution. For the lift, here defined as the aerodynamic force normal to the airfoils' chord, the local pressure is taken as constant along a line between the middle of two neighbouring pairs of sensors. The resulting local force is acting normal to the local surface that is inclined with respect to the airfoils' center line. Thus, with $x$ being here the chordwise coordinate and $z_u, z_l$ the contour coordinate of upper and lower surface, the aerodynamic lift $L$ and moment about quarter chord $M_{0.25}$ are evaluated via the following formula. Results are presented in the following sections.

$$L = \int_0^c \left[ P_l(x) \cos\left(\frac{\partial z_l(x)}{\partial x}\right) - P_u(x) \cos\left(\frac{\partial z_u(x)}{\partial x}\right) \right] dx$$

$$M_{0.25} = \int_0^c \left[ P_u(x) \cos\left(\frac{\partial z_u(x)}{\partial x}\right) - P_l(x) \cos\left(\frac{\partial z_l(x)}{\partial x}\right) \right] (0.25 - x) dx$$

# 3 Low Speed BVI

The low speed flight condition repr sents a 6° descent flight, that is known to produce large BVI-induced noise. Thus, the BVI-induced pressure fluctuations are large, especially in areas, where the vortices are almost parallel to the blades. In this case, the noise sources can be located in Fig. 2 between $\psi = 45°$ and 65° on the advancing side and between $\psi = 290°$ and 305° on the retreating side. The figure shows the peak-to-peak differences in pressure to be very large. The advancing side shows smaller pressure differences than the retreating side, even though the blade-vortex distance must be about the same. This is partly due to the larger Mach number on the advancing blade as explained before.

## 3.1 Vortex Locations

The vortex locations for this test case are shown in Fig. 2, where the traces of BVI are clearly visible. This is where the vortices are relatively close to the blade and where the angle $\beta$ is not too large. It must be noted that $\beta$ is large (almost 90°) in the front region of the disk which would induce only low frequency fluctuations in the pressure at a constant radius. These were filtered out by the procedure described above and are not visible here. Additionally, in this region the vortices are positioned significantly above the rotor plane and thus are not inducing pressure changes with locally large gradients.

On the advancing side at $\psi \approx 60°$ some irregularities can be found in Fig. 2. This might be due to some roll-up processes of the oncoming vortices in the vicinity of the blade. At the rear of the disk between $\psi = 340°$ and $\psi = 10°$ some disturbances appear. They are due to the rotor hub wake, distorting the rotors' vortex wake system. Additionally, the tip vortices are quickly travelling below the rotor and thus are not able to induce any significant local pressure gradients in the rotor plane.

## 3.2 Vortex Core Radius

The method to measure the vortex core radius was discussed in section 2.3. This method is useful only where the vortices are very close to the blade (otherwise the apparent core radii will appear too large) and where the angle $\beta$, with which the vortices are interacted, is smaller than about 40°. However, there are enough BVI events available to satisfy the objectives. The problem mainly is in a correct identification of the angle $\beta$ from Fig. 4 and all the $\Delta\psi$ from the time history of each radial section. Where the vortices are not close to the blades $\Delta\psi$ is difficult to obtain. On the other hand, the effective $\Delta\psi$ indicates the vertical distance between the blade and a vortex following the Biot-Savart law.

Two more BVI events on the advancing side are investigated here, see Fig. 3 (bottom graph). At radial position $x = 0.6$, a close encounter can be found at $\psi_{BVI} = 32.3°$, Fig. 2, where $\Delta\psi = 5.4°$ and $\beta \approx 35°$ from Fig. 4. The result here is $r_c/c \approx 0.44$. Here the vortex was generated at about $\psi = 160°$ from the blade currently being at $\psi = 112.3°$ and the vortex age is 680°. Thus, although the vortex is very close to the rotor disk, its core radius is much larger than in the example before. A third example: at $x = 0.94$ and $\psi_{BVI} = 67.7°$, Fig. 2, we find $\Delta\psi = 2.1°$ from Fig. 3 (middle graph) and $\beta \approx 45°$ from Fig. 4. This gives $r_c/c \approx 0.23$. Here the vortex was created at $\psi = 120°$ by the same blade and is 308° old. Thus, its age and size fit well to the first example and additionally, the widening of the core radius with time can be assumed to be about 0.2 chord per 300° of vortex age. Of course, for validation of this assumption much more BVI events have to be investigated. This analyses is useful only at those events which show a very close blade-vortex distance, visible by the largest pressure peak-to-peak amplitudes. There are usually only few of these available. For other BVI locations, the results are given in Table 1.

### 3.3 Reduced Frequencies

With the approximation of the induced velocity field of a BVI event to be close to sinusoidal for the airfoil, then the wave length is twice the distance between the two corresponding pressure peaks, $\Delta\psi$. Thus, the frequency of a BVI event is $\omega = 2\pi\Omega/(2\Delta\psi)$. With this, the reduced frequency of a BVI event is

$$k = \frac{\omega c}{2V} = \frac{\pi}{\Delta\psi}\frac{c/(2R)}{x + \mu\sin\psi_{BVI}} = \frac{\pi k_t}{\Delta\psi(x + \mu\sin\psi_{BVI})}$$

As an example, for the model rotor the reduced frequency of the tip in hover, $k_t = 0.03025$, is not very large and justifies quasisteady assumptions. Now, $\Delta\psi$ usually is very small and $x$ is smaller than one. Using the BVI envent mentioned in section 2.3 with $x = 0.99$, $\psi_{BVI} = 295.5^o$ and $\Delta\psi = 1.9^o$, the local reduced frequency is about $k = 3.4$. No quasisteady assumptions can be used for simulation purposes. Note that this BVI event primarily is a sine wave that is only $2\Delta\psi r/c = 1.08$ chords long, so at some instances of time both pressure peaks are present on the airfoil with a distance of 0.54 chords. The corresponding results for the other two examples mentioned before (section 3.2) are: at $\psi_{BVI} = 67.7^o, x = 0.94$ the reduced frequency is $k = 2.4$ and the wavelength is 1.13 chords long. At $\psi_{BVI} = 32.3^o, x = 0.6$, we find $k = 1.5$ and a wavelength of about 1.9 chords.

### 3.4 Blade Loading

Following the integration procedure described in section 2.4, the aerodynamic lift and moment about the quarter chord can be calculated at the three radial sections $x = 0.75, 0.87, 0.97$. It should be noted that the steady part includes some uncertainties because of the manual correction of the offsets of most of the sensor signals, however the dynamic parts are not affected. Fig. 6 (top) shows the lift distribution without filtering, below the first 10 harmonics are subtracted to compare with the leading edge pressure data of Fig. 2.

The total lift in the top graph shows a small region of negative lift at the blades' tip between $\psi = 150^o$ and $180^o$. Additionally, the radial gradient of lift is not large, so the tip vortex will form more inboard than at the tip which might be a reason for the discrepancies in the prediction of the BVI trajectories and experiment as shown in Fig. 2. The prediction assumes the tip vortex always to form at the tip and not inboard.

The graph at the bottom of Fig. 6 shows very clearly the BVI induced lift fluctuations, and the vortex trajectories from Fig. 2 again are exactly in the middle between two corresponding peaks as has been in the leading edge pressure distribution. Thus, the lift is directly proportional to the leading edge pressure without a time lag. This is to be expected since the lift results mainly from the pressure difference in the first half of the airfoil.

Fig. 7 gives insight into the aerodynamic moment (about quarter chord) development during one revolution; on top, the unfiltered data and below the first 10 harmonics are subtracted. From the unfiltered data the effect of transonic Mach numbers can be seen at the tip around $\psi = 90^o$, where the moment is negative. There the center of pressure is moving aft of the quarter chord point, producing a nose-down moment. Below, the filtered data again show very clearly the various BVI induced loadings. However, there is a certain time delay between the vortex trajectories as identified from the leading edge pressure and the resulting aerodynamic moment development. This can be explained by the fact that the pressure data are multiplied with $(x - 0.25)$ and thus the effects of large pressure differences at the leading edge are reduced while small pressure differences at the trailing edge are amplified. So it takes some time for the changes in pressure to produce a change in the aerodynamic moment about quarter chord.

## 4 High Speed BVI

This test condition is characterised by an advance ratio of $\mu = 0.314$, $\alpha_S = -0.94^o$ and $C_T/\sigma = 0.058$. This flight condition is interesting since there are strong BVI effects found at azimuth angles from $90^o$ to $150^o$ and from $270^o$ to $300^o$. Fig. 8 shows the pressure at 3% upper chord in analogy to Fig. 1. In the upper part, a large 1/rev variation in the pressure signals can be seen due to the large fluctuation in the local Mach number. The tip Mach number varies from 0.87 at $\psi = 90^o$ to 0.46 at $270^o$. Strong BVI effects can be found in the regions mentioned above with peak-to-peak amplitudes very similar to those found in Fig. 1. The number of BVI events in the lower part of Fig. 8 are less than can be found in Fig. 1 since the wake is convected by twice the velocity of the low speed case. Again, the average time history is very close to the single revolution except in the rear of the disk where the hub wake interacts with the blades.

## 4.1 Vortex Locations

From the pressure sensor signals at 3% upper chord the BVI locations can be clearly seen, when subtracting the first 6 harmonics, see Fig. 8 (lower part). Surprisingly, the BVI locations to be expected show an opposite time history on the advancing side, compared to the low speed BVI case. First an upwash is encountered, than a downwash, indicating a vortex having a negative circulation. Also, there are more vortex interactions between these locations with an opposite time history, as if there are secondary vortices with positive circulation, obviously created at a more inboard station than at the tip. All of these BVI locations can be clearly seen in Fig. 9, where again the first 6 harmonics are subtracted from the time history. The BVI locations on the advancing side, where the circulation is positive, are marked by a dashed line. They are inbetween the tip vortex locations and have been identified by a pressure time history to be first down, then up (as they were in the low speed BVI case, see Fig. 1). Also, the results from the wake program [7] already used for the prediction in Fig. 2 are given. The BVI locations at this large advance ratio are predicted almost exactly. Additionally, the region of negative lift (as evaluated in a later section) is marked by the shaded area. It can be seen that the strongest BVI on the advancing side takes place where the lift is almost zero.

## 4.2 Vortex Core Radius

Based on the BVI induced pressure fluctuations in Fig. 9, the smallest blade-vortex distance was found to be at $x = 0.9$, $\psi_{BVI} = 93.6°$ and $\Delta\psi = 2.5°$, (the time history is given in Fig. 10). To evaluate $\beta$, the instantaneous vortex positions at the various azimuth must be known. For this, Fig. 11 shows these vortex trajectories at different azimuth (top graphs) and an overview of the BVI locations with the various vortex trajectories at the BVI location. The value of $\beta$ is about 70° from Fig. 11 and is rather large. The result is a core radius of about 15% chord that is surprisingly well within the earlier evaluated data. It has to be noted that this vortex is relatively young. It was created at $\psi = 117°$ from th blade being currently at 183.6° and thus the vortex is only 67° old. Another example: at $x = 0.99$, $\psi_{BVI} = 291.2°$ the value of $\Delta\psi$ is 3.8° from Fig. 10. The angle $\beta$ is about 40° from Fig. 11 and thus a vortex core radius of 28% chord can be calculated. This vortex was created at $\psi = 248°$ from the blade being at $\psi = 21.2°$ and its age is 133°. Again the result agrees well with those obtained from the low speed case.

As mentioned before, on the advancing side double vortex systems can be found. One of these at $x = 0.8$ around $\psi = 38°$ is shown in Fig. 10 (top graph). The tip vortex with negative circulation is indicated with the index '2' and the secondary, more inboard created vortex with positive circulation is indicated with '1'. For event '2' we find $\psi_{BVI} = 40.6°$, $\Delta\psi = 1.6°$ and $\beta \approx 1.6°$ so a core radius of 23% chord is the result. The vortex was created at $\psi = 150°$ from the same blade's tip and is 250.6° old. The other event, '1', has the following data: $\psi_{BVI} = 45.6°$, $\Delta\psi = 2°$ and $\beta \approx 12°$. A core radius of 28% is the result. Again, this vortex is created from the same blade, but at a more inboard station of $x \approx 0.9$ at the same azimuth and thus the vortex age is about the same as for event '2'.

## 4.3 Reduced Frequencies

As in the low speed BVI case, the reduced frequencies of the various BVI events can be calculated. For the examples just given, the local reduced frequencies are at $x = 0.9$, $\psi_{BVI} = 93.6°$: $k = 1.8$; at $x = 0.99$, $\psi_{BVI} = 291.2°$: $k = 2.1$. On the advancing side for event '2': $k = 3.4$ and for event '1': $k = 2.77$. Again, these values are about the same as in the low speed BVI case.

## 4.4 Blade Loading

After having corrected the static offset in the pressure signals manually, the integration over chord gives the aerodynamic lift and the aerodynamic moment about quarter chord. The total lift distribution is presented in Fig. 12. A large negative lift area can be found between $\psi = 85°$ and 178° with the peak negative lift at $\psi = 140°$. All of the outer 25% radius has negative lift and thus it is clear that the tip vortex will have negative circulation. Also, a secondary vortex will form here at $x \approx 0.75$ with positive circulation since the radial gradient of the blade loading is large. Because of the large 1/rev and 2/rev lift amplitudes in the total lift, BVI induced lift fluctuations are hardly visible here. Thus, the first 6 harmonics are subtracted and the result is given below in Fig. 12. All of the vortex induced loadings are clearly visible now and the peak-to-peak lift fluctuations are very comparable to those of the low speed BVI case, Fig. 6. The BVI locations obtained from Fig. 9 are added to the figure and it is to be seen that there are no phase lags between BVI location and lift development.

Fig. 13 gives an impression of the aerodynamic moment. The total aerodynamic moment about quarter chord is shown on top. Although the low frequency amplitudes are larger than in the low speed case (see Fig. 7), the

BVI impact on the moment is clearly visible. In the first quadrant at the tip strong negative moments appear, mostly due to transonic effects moving the center of pressure aft of the quarter chord point. This area is ended with the interaction of the vortex from the blade before. Since this vortex first induces an upwash, the negative moment extends to more inboard regions ($\psi = 85°$ to $120°$). Then, the lift changes to negative lift (see Fig. 12) so the transonic effects produce positive moments from then on.

The BVI impact on the moment is more visible when subtracting the first 6 harmonics from the data. This is done in Fig. 13, lower graph. Strong negative moments appear at the upwash side of the BVI events, followed by a positive moment. In addition to the moment, the BVI locations obtained from the leading edge sensors are indicated. A small time delay between the BVI location and the response of the aerodynamic moment can be found while the lift does not show a time delay as mentioned before.

# 5 Summary and Conclusions

A hingeless BO105 40% Mach-scaled model rotor was instrumented with 124 pressure transducers and 32 strain gages on one blade. Experiments were made in the German-Dutch Windtunnel in 1992, concentrating especially on BVI configurations. Two of the test runs are presented and analysed in this paper; a low speed BVI case at $\mu = 0.149$ and a high speed BVI case at $\mu = 0.314$, both representing descent flight conditions with a high noise level. From the pressure data at 3% upper chord the BVI locations are identified and the intensity of BVI induced pressure oscillations indicates the proximity of the vortex to the blade. From these data, the vortex core radii have been evaluated to a certain degree of accuracy and are found to be in the range of 20% chord, growing with the vortex age. The reduced frequencies of the BVI locations under investigation were found to be between $k = 1.8$ and $k = 3.4$, therefore no quasisteady assumptions can be made for puposes of simulation of these effects.

The low speed BVI is characterised by very strong BVI at the blade tip, $\psi = 295°$ azimuth (retreating side) and on the advancing side between $\psi = 35°$ and $65°$ over all radial positions. This results in an extreme noise producing state, known as blade slap. The vortices in the front of the disk have a larger distance to the disk and do not strongly affect the pressure distribution. Since the lift is positive almost everywhere on the disk, the tip vortices always have positive circulation. In contrast to this, the high speed BVI case shows a large negative lift area between $\psi = 85°$ and $180°$, producing a tip vortex in this area with negative circulation. Thus, the time history of pressure on the advancing side is opposite than what was found in the low speed BVI case. In addition, the radial gradient from negative lift to positive lift more inboard is strong enough to produce a second vortex with positive circulation at a more inboard location. This vortex also produces BVI effects on the advancing side that are clearly visible in the pressure time histories.

The lift development is found to have no time delay with respect to the leading edge pressure time history at 3% chord, while the aerodynamic moment time history shows a time delay of up to 2° azimuth. This is because for the aerodynamic moment about quarter chord the leading edge pressure is not that important while pressure changes at the trailing edge are. Thus, the aerodynamic moment is changing while the vortex induced pressures reach the trailing edge.

A simulation of the BVI locations shows good agreement in the high speed case but in the low speed case, the simulated BVI locations are generally predicted to be too far in the front of the disk. One explanation may be found in the lift distribution: in the front of the disk the total lift is close to zero and the radial gradients are not large. This may lead to a tip vortex forming not at the tip but more inboard, shifting the BVI locations in downstream direction.

# References


[1] W.R. Splettster, K.J. Schultz, B. Junker, W. Wagner, B. Weitemeier, "The HELINOISE Aeroacoustic Rotor Test in the DNW," *DLR-Mitt. 93-09*, Braunschweig, 1993

[2] D.A. Boxwell, F.H. Schmitz, W. Spletster, K.J. Schultz, "Model Helicopter Rotor High Speed Impulsive Noise: Measured Acoustic and Blade Pressures," *9th European Rotorcraft Forum*, Stresa, Italy, 1983

[3] Y.H.Yu, A.J. Landgrebe, S.R. Liu, P.F. Lorber, M.J. Pollack, R.M. Martin, D.E. Jordan, "Aerodynamic and Acoustik Test of a United Technologies Model Scale Rotor at DNW," *46th Annual Forum of the American Helicopter Society*, Washington, D.C., 1990

[4] M.K. Lal, S.G. Liou, G.A. Pierce, M.M. Komerath, "Measurements of Unsteady Pressure on a Pitching Rotor Blade," *49th Annual Forum of the American Helicopter Society*, St. Louis, Missouri, 1993

[5] B. Gelhaar, B. Junker, W. Wagner, "DLR - Rotor Teststand Measures Unsteady Rotor Aerodynamic Data," *19th European Rotorcraft Forum*, Como, Italy, 1993

[6] W.R. Splettster, G. Niesl, D.G. Papanikas, F. Cenedese, F. Nitti, "Experimental Results of the European Helinoise Aeroacoustik Rotor Test in the DNW," *19th European Rotorcraft Forum*, Como, Italy, 1993

[7] T.S. Beddoes, "A Wake Model for High Resolution Airloads," *International Conference on Rotorcraft Basic Research*, Research Triangle Park, NC, 1985

| psi_BVI (deg) | Del_psi (deg) | beta (deg) | r_c/c (-) |
|---|---|---|---|
| r/R = 0.60: | | | |
| 32.3 | 5.4 | 34.0 | 0.44 |
| 48.0 | 4.3 | 6.0 | 0.44 |
| 63.6 | 2.8 | 9.0 | 0.29 |
| 77.0 | 9.2 | 31.0 | 0.85 |
| 289.2 | 10.5 | 4.0 | 0.69 |
| 313.5 | 9.0 | 29.0 | 0.56 |
| r/R = 0.70: | | | |
| 35.2 | 5.0 | 27.0 | 0.50 |
| 48.3 | 3.5 | 0.0 | 0.41 |
| 62.4 | 2.3 | 16.0 | 0.27 |
| 74.4 | 6.0 | 35.0 | 0.60 |
| 264.0 | 10.0 | 30.0 | 0.69 |
| 286.4 | 8.0 | 6.0 | 0.64 |
| 306.0 | 7.0 | 20.0 | 0.55 |
| r/R = 0.80: | | | |
| 36.5 | 5.0 | 25.0 | 0.58 |
| 47.8 | 4.5 | 1.0 | 0.59 |
| 60.7 | 3.5 | 25.0 | 0.43 |
| 71.5 | 3.8 | 35.0 | 0.42 |
| 271.8 | 7.5 | 28.0 | 0.62 |
| 289.0 | 6.0 | 13.0 | 0.56 |
| 303.5 | 4.4 | 13.0 | 0.42 |
| r/R = 0.90: | | | |
| 24.7 | 2.5 | 38.0 | 0.27 |
| 37.0 | 7.0 | 15.0 | 0.97 |
| 47.2 | 4.5 | 6.0 | 0.65 |
| 55.8 | 2.0 | 14.0 | 0.29 |
| 68.2 | 3.0 | 39.0 | 0.35 |
| 292.5 | 3.3 | 16.0 | 0.35 |
| 303.0 | 4.5 | 6.0 | 0.50 |
| r/R = 0.99: | | | |
| 37.6 | 2.7 | 12.0 | 0.41 |
| 46.6 | 3.3 | 9.0 | 0.52 |
| 53.4 | 1.6 | 21.0 | 0.24 |
| 62.8 | 2.0 | 32.0 | 0.27 |
| 66.5 | 2.8 | 39.0 | 0.35 |
| 77.9 | 3.1 | 63.0 | 0.23 |
| 295.5 | 1.9 | 22.0 | 0.22 |
| 304.5 | 4.0 | 2.0 | 0.50 |
| 316.7 | 5.8 | 18.0 | 0.71 |

| psi_BVI (deg) | Del_psi (deg) | beta (deg) | r_c/c (-) |
|---|---|---|---|
| r/R = 0.60 | | | |
| 33.6 | 4.0 | 25.0 | 0.40 |
| 39.6 | 2.5 | 17.0 | 0.28 |
| 57.0 | 2.0 | 3.0 | 0.25 |
| 75.4 | 2.2 | 25.0 | 0.26 |
| 95.5 | 3.5 | 56.0 | 0.26 |
| 269.7 | 8.0 | 19.0 | 0.31 |
| r/R = 0.70 | | | |
| 35.3 | 3.5 | 17.0 | 0.43 |
| 40.1 | 2.2 | 13.0 | 0.28 |
| 72.0 | 2.5 | 32.0 | 0.31 |
| 87.1 | 2.8 | 51.0 | 0.26 |
| 90.5 | 1.6 | 55.0 | 0.13 |
| 276.4 | 5.5 | 19.0 | 0.29 |
| r/R = 0.80 | | | |
| 35.6 | 2.0 | 12.0 | 0.28 |
| 40.6 | 1.6 | 8.0 | 0.23 |
| 52.8 | 2.0 | 11.0 | 0.30 |
| 61.3 | 2.5 | 23.0 | 0.36 |
| 68.6 | 1.6 | 35.0 | 0.21 |
| 79.9 | 3.1 | 48.0 | 0.33 |
| 110.8 | 3.5 | 78.0 | 0.11 |
| 281.8 | 3.5 | 24.0 | 0.23 |
| r/R = 0.90 | | | |
| 35.6 | 2.2 | 10.0 | 0.34 |
| 50.9 | 2.2 | 14.0 | 0.35 |
| 64.5 | 2.5 | 35.0 | 0.35 |
| 72.4 | 2.3 | 49.0 | 0.26 |
| 78.5 | 2.0 | 55.0 | 0.20 |
| 93.6 | 2.5 | 70.0 | 0.15 |
| 287.0 | 4.2 | 27.0 | 0.32 |
| r/R = 0.99 | | | |
| 25.0 | 5.2 | 40.0 | 0.65 |
| 35.3 | 2.4 | 7.0 | 0.40 |
| 39.6 | 1.0 | 5.0 | 0.17 |
| 48.6 | 2.4 | 15.0 | 0.41 |
| 56.0 | 1.2 | 29.0 | 0.19 |
| 62.0 | 1.3 | 37.0 | 0.19 |
| 66.5 | 2.3 | 48.0 | 0.29 |
| 80.0 | 3.5 | 67.0 | 0.26 |
| 291.2 | 3.8 | 42.0 | 0.28 |

Table 1: BVI core radius evaluation. $\mu = 0.149$, $\alpha_S = +5.05°$ (left table) and $\mu = 0.314$, $\alpha_S = -0.9°$ (right table). $C_T/\sigma = 0.058$ in both cases.

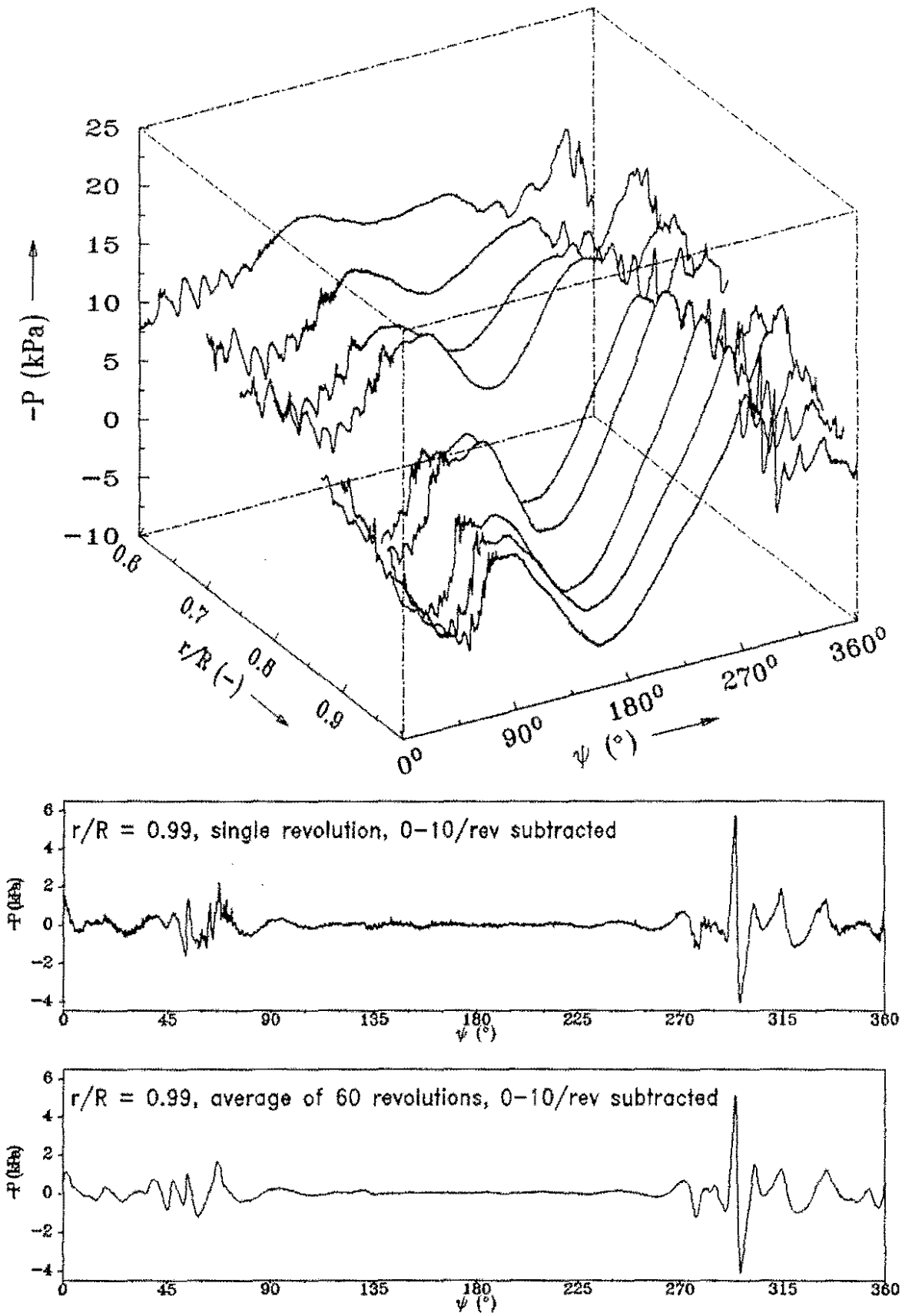


Figure 1: Leading edge pressure time history at $r/R = 0.6, 0.7, 0.75, 0.8, 0.87, 0.9, 0.94, 0.97, 0.99$. Sensor position: 3% chord, upper side. $\mu = 0.149$, $\alpha_S = +5.05°$, $C_T/\sigma = 0.058$.

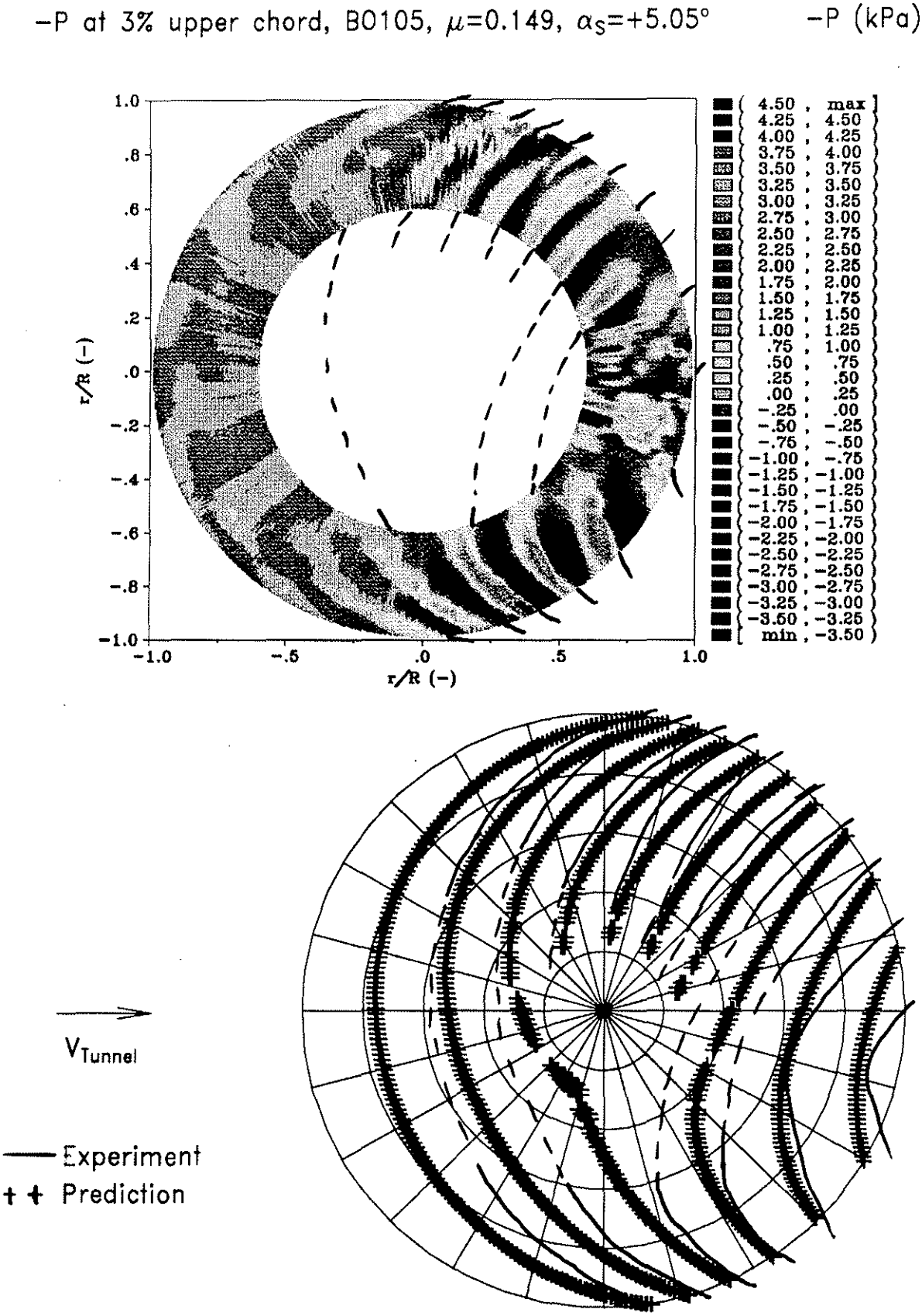


Figure 2: Leading edge pressure distribution (first 10 harmonics subtracted) and BVI locations in the rotor disk. Sensor position: 3% chord, upper side. Comparison of theory (Beddoes' wake model) and experiment below. $\mu = 0.149$, $\alpha_S = +5.05°$, $C_T\sigma = 0.058$.

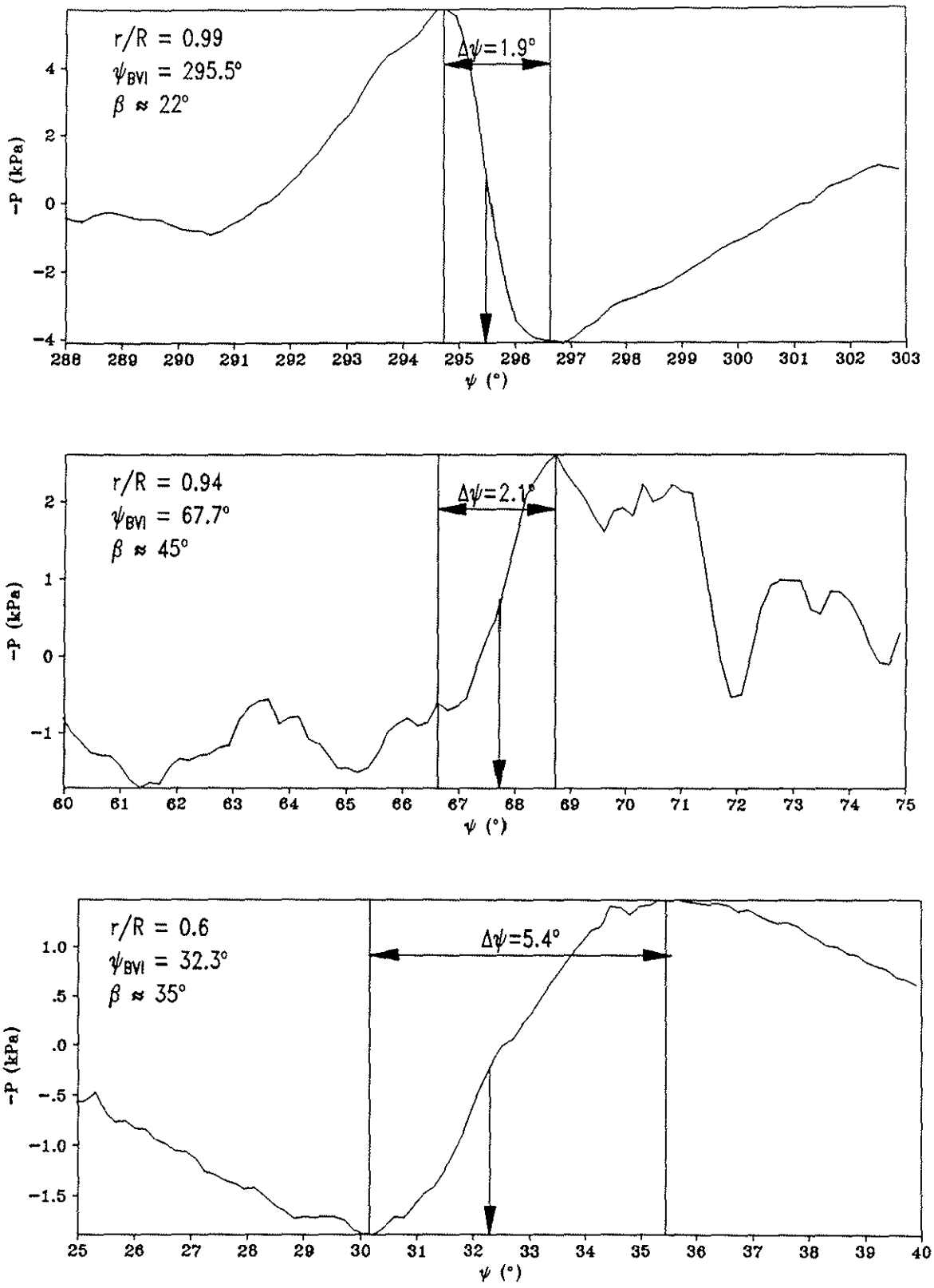


Figure 3: Leading edge pressure time history at selected locations for vortex core radius evaluation. Sensor position: 3% chord, upper side. $\mu = 0.149$, $\alpha_S = +5.05°$, $C_T/\sigma = 0.058$.

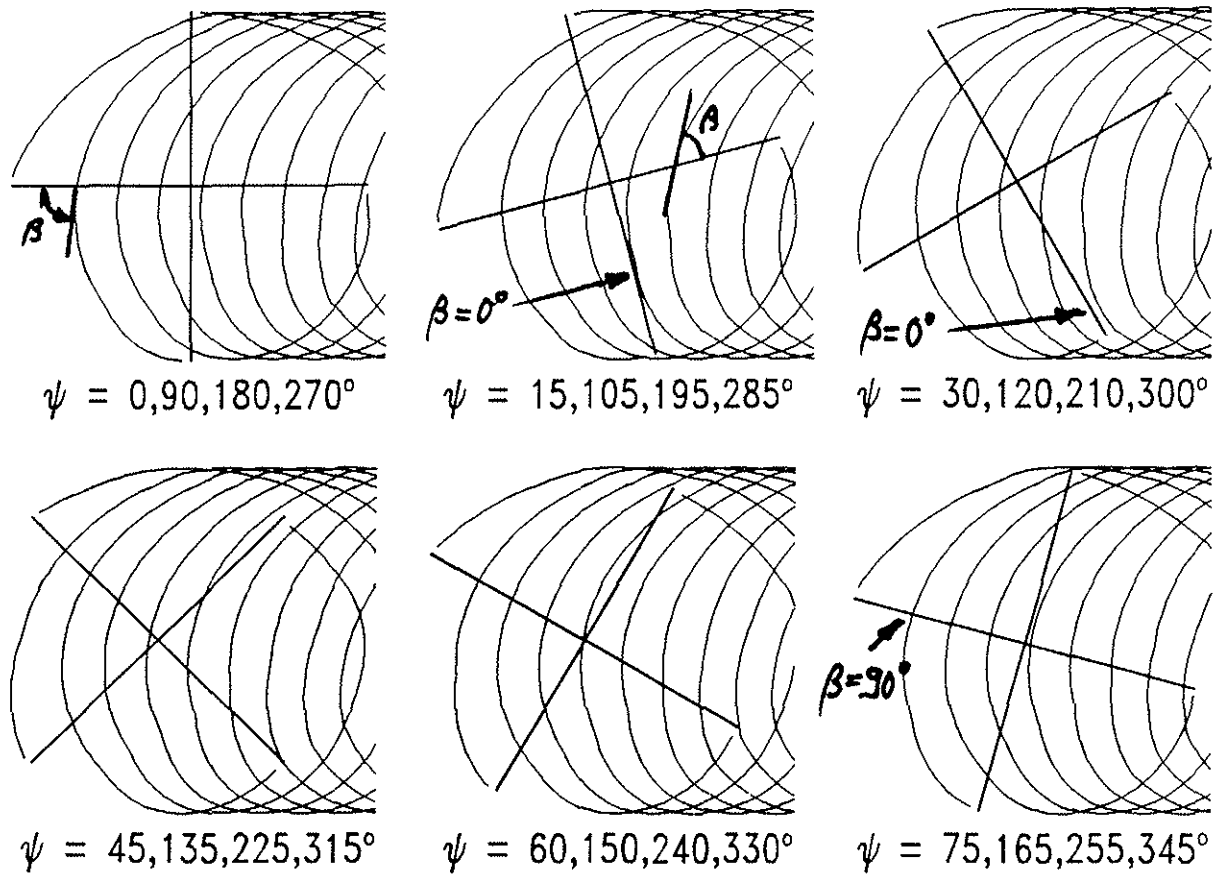


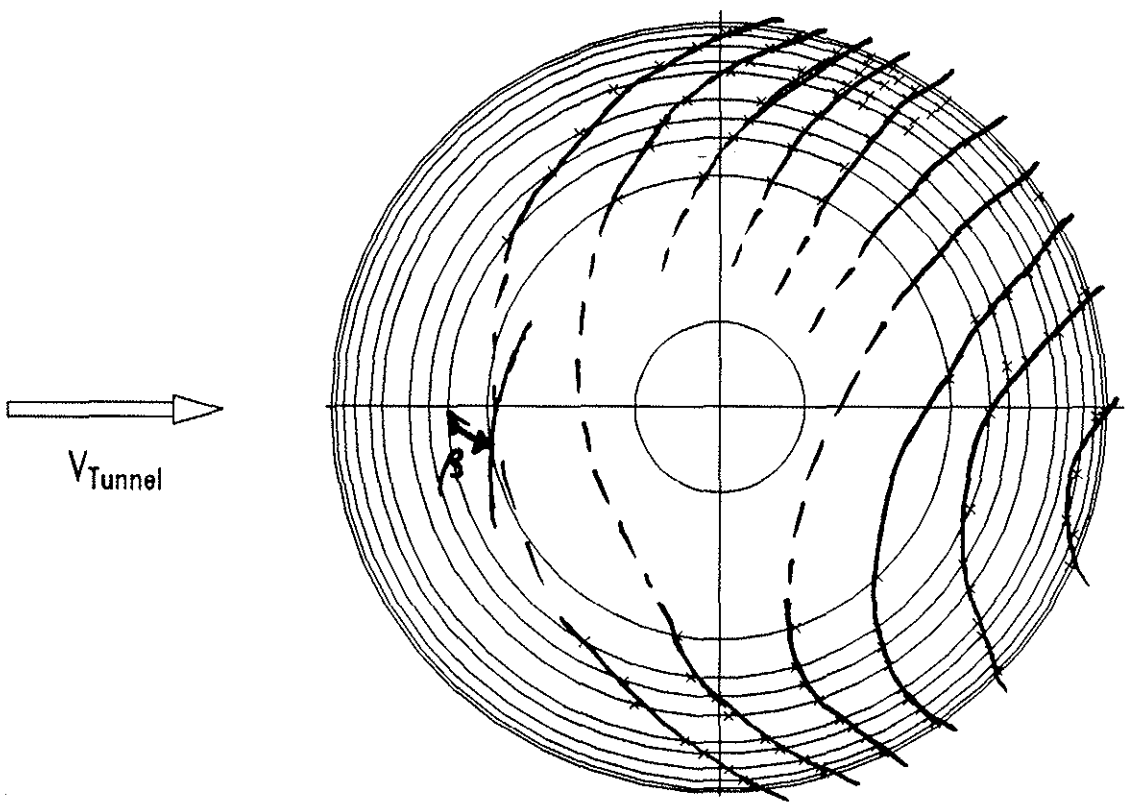


Figure 4: Wake geometry and instantaneous vortex positions at various BVI locations for identification of the angle $\beta$. $\mu = 0.149$, $\alpha_S = +5.05°$, $C_T/\sigma = 0.058$.

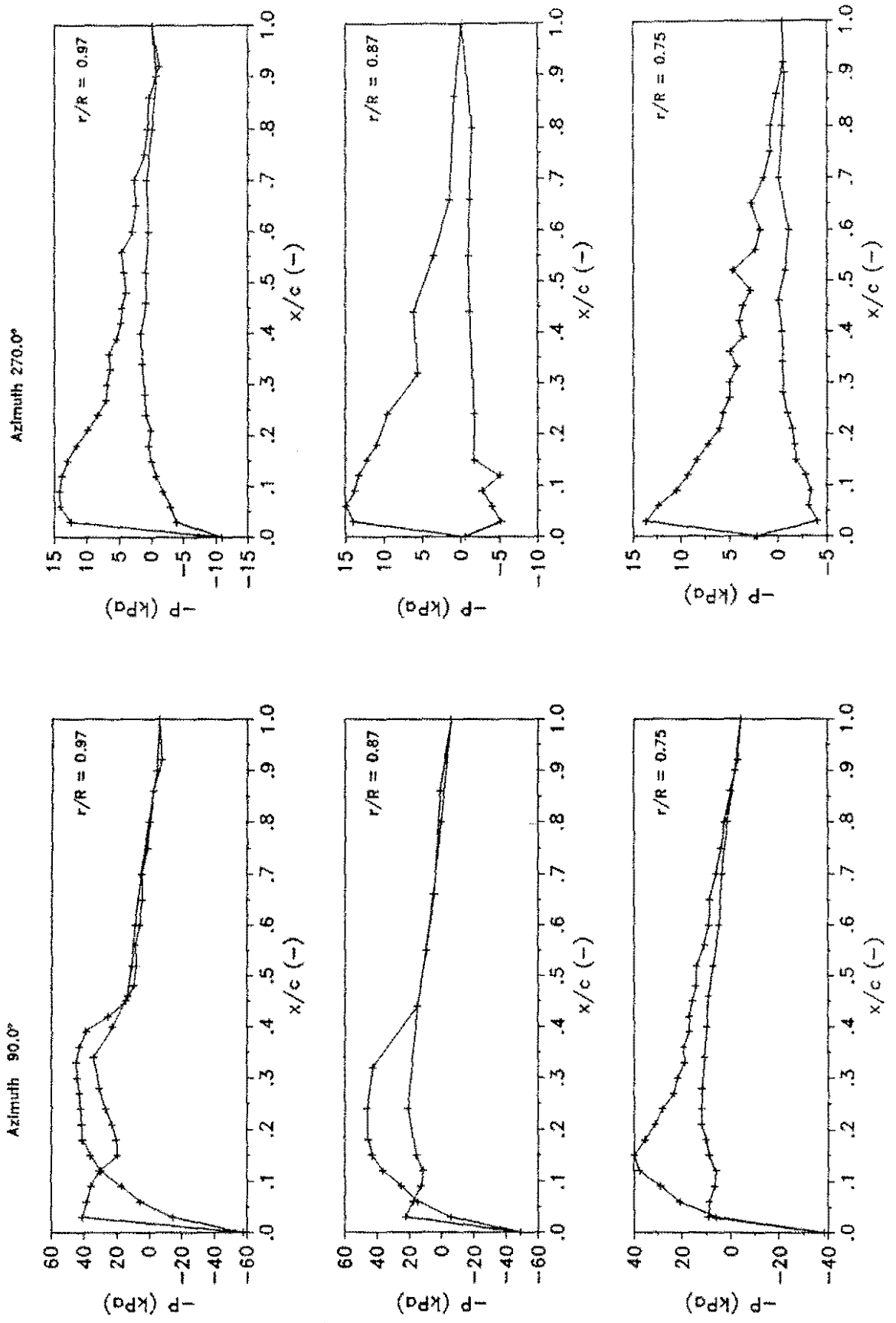


Figure 5: Chordwise pressure distributions at selected azimuth. $\mu = 0.314$, $\alpha_S = -0.9°$, $C_T/\sigma = 0.058$.

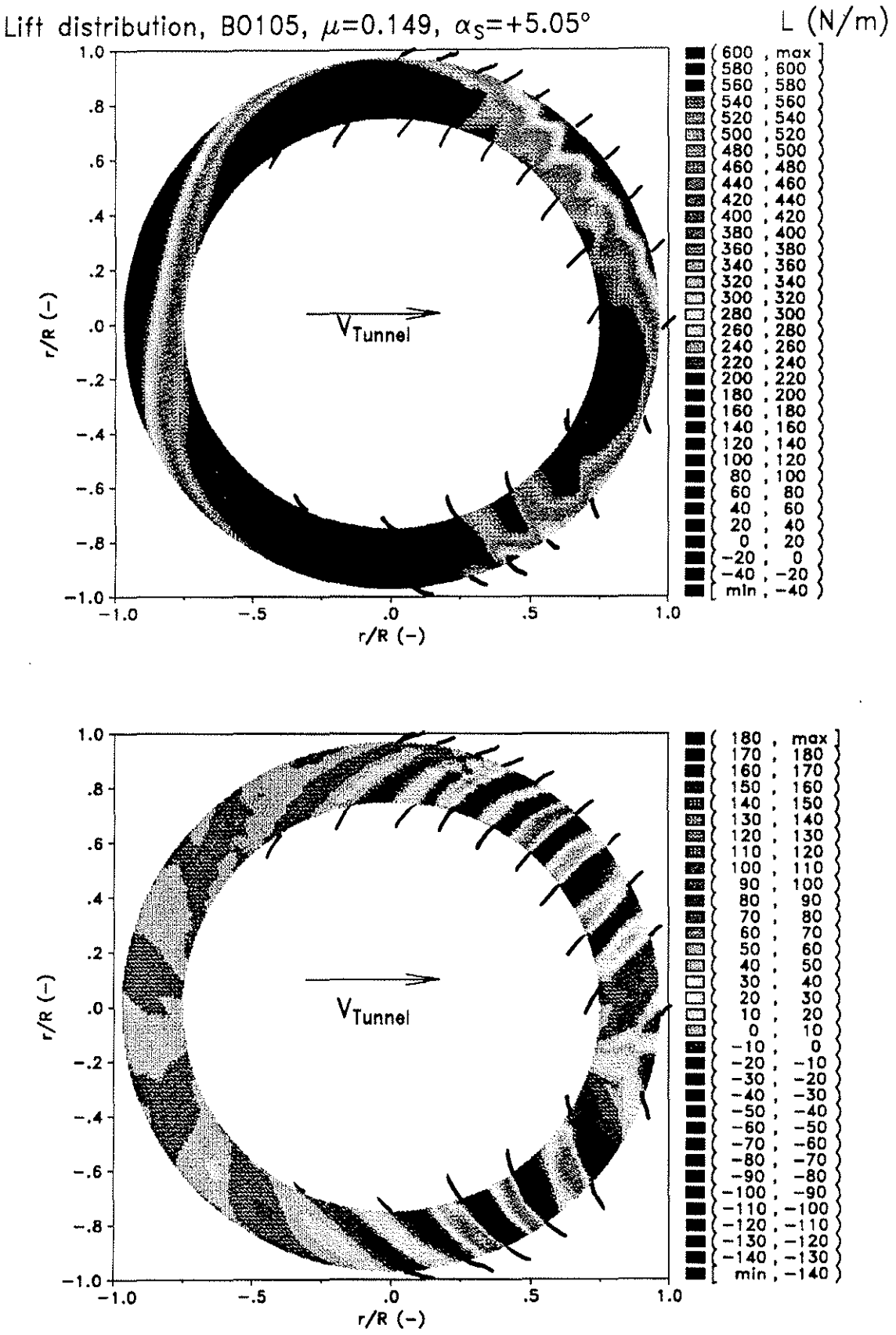


Figure 6: Aerodynamic lift distribution, unfiltered (top) and the first 10 harmonics subtracted (below). $\mu = 0.149$, $\alpha_S = +5.05°$, $C_T/\sigma = 0.058$.

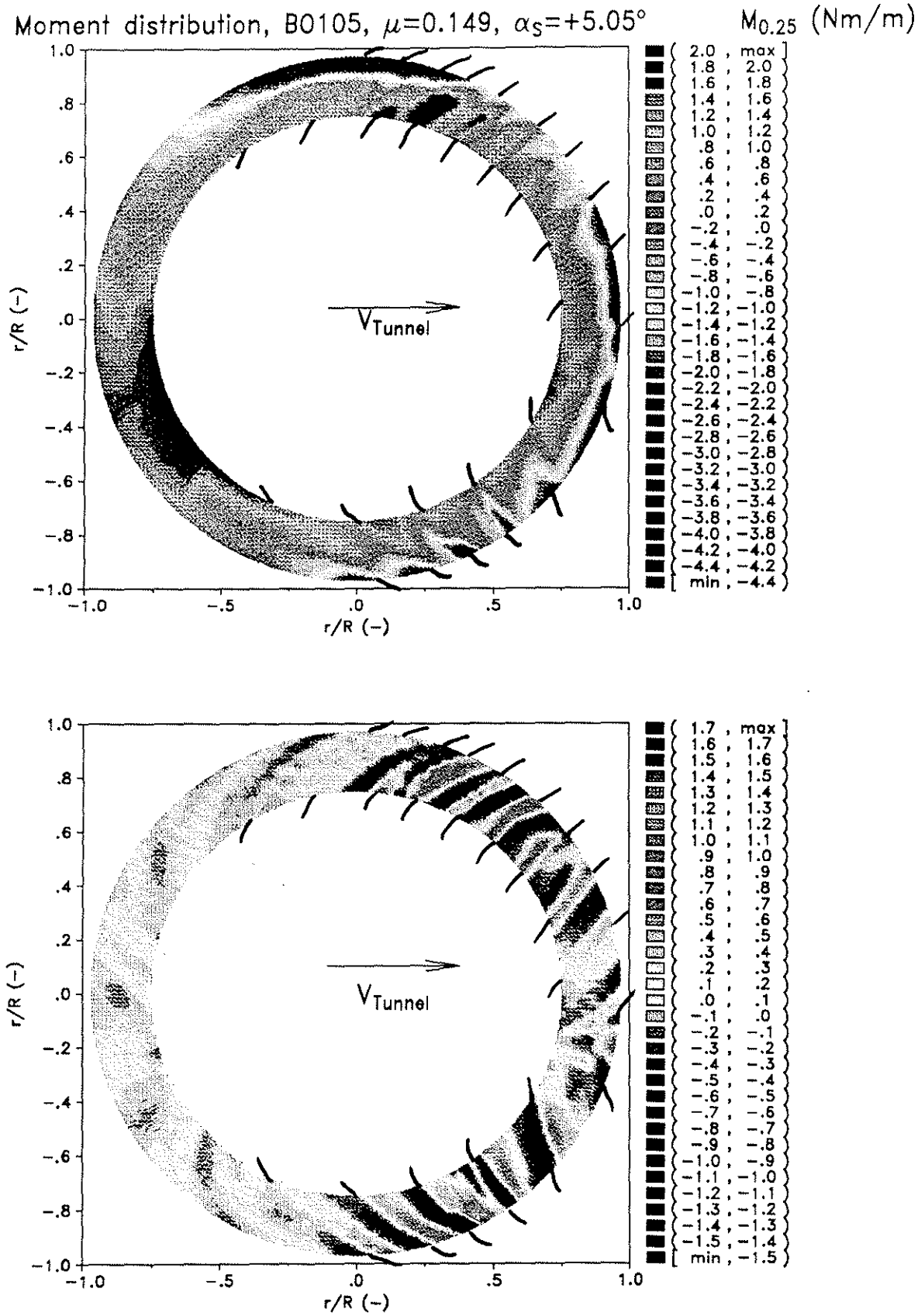


Figure 7: Aerodynamic moment distribution about $c/4$, unfiltered (top) and the first 10 harmonics subtracted (below). $\mu = 0.149$, $\alpha_S = +5.05°$, $C_T/\sigma = 0.058$.

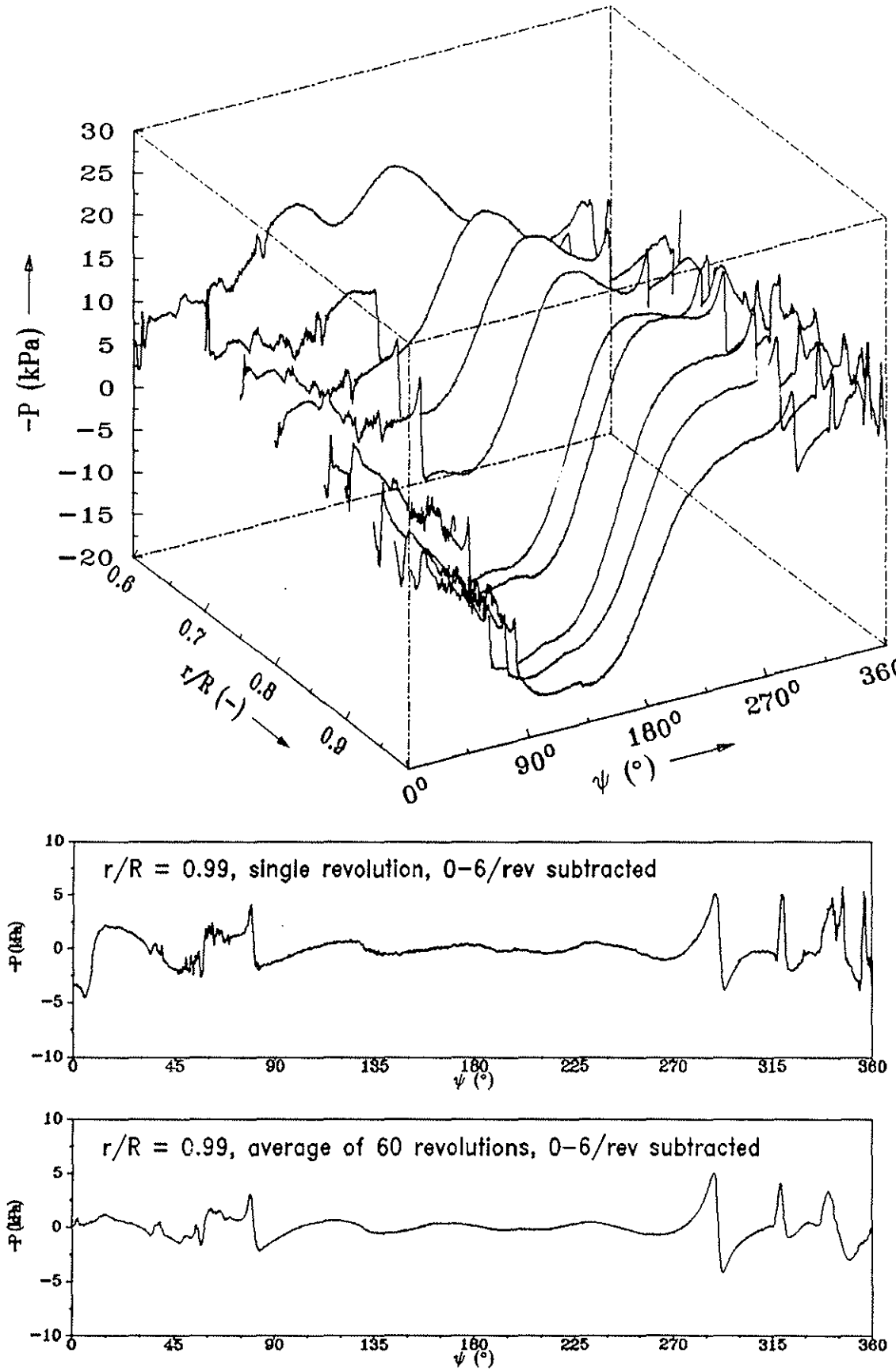


Figure 8: Leading edge pressure time history at $r/R = 0.6, 0.7, 0.75, 0.8, 0.87, 0.9, 0.94, 0.97, 0.99$. Sensor position: 3% chord, upper side. $\mu = 0.314$, $\alpha_S = -0.9°$, $C_T/\sigma = 0.058$.

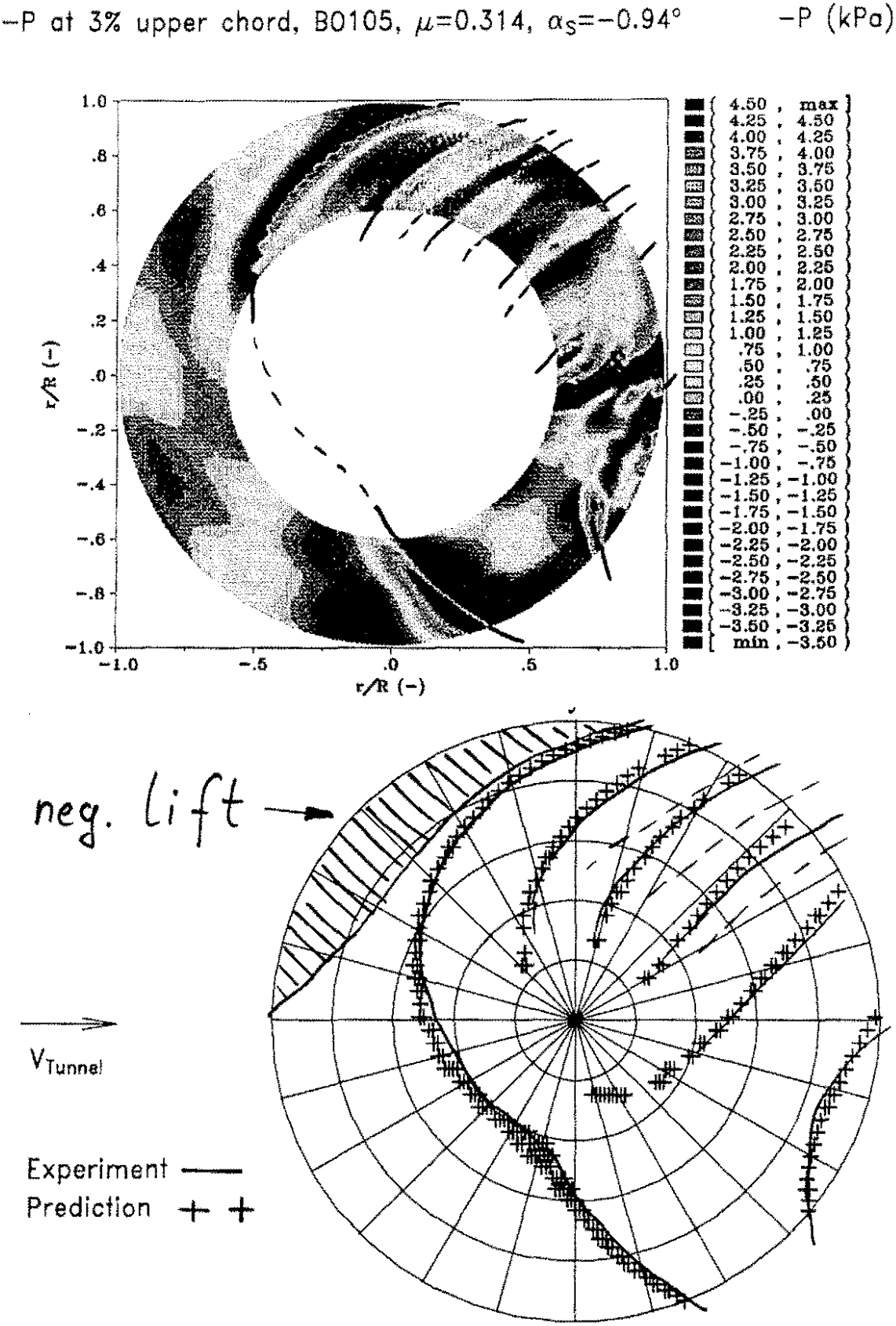


Figure 9: Leading edge pressure distribution (first 6 harmonics subtracted) and BVI locations in the rotor disk. Sensor position: 3% chord, upper side. Comparison of theory (Beddoes' wake model) and experiment below. $\mu = 0.314$, $\alpha_S = -0.9°$, $C_T/\sigma = 0.058$.

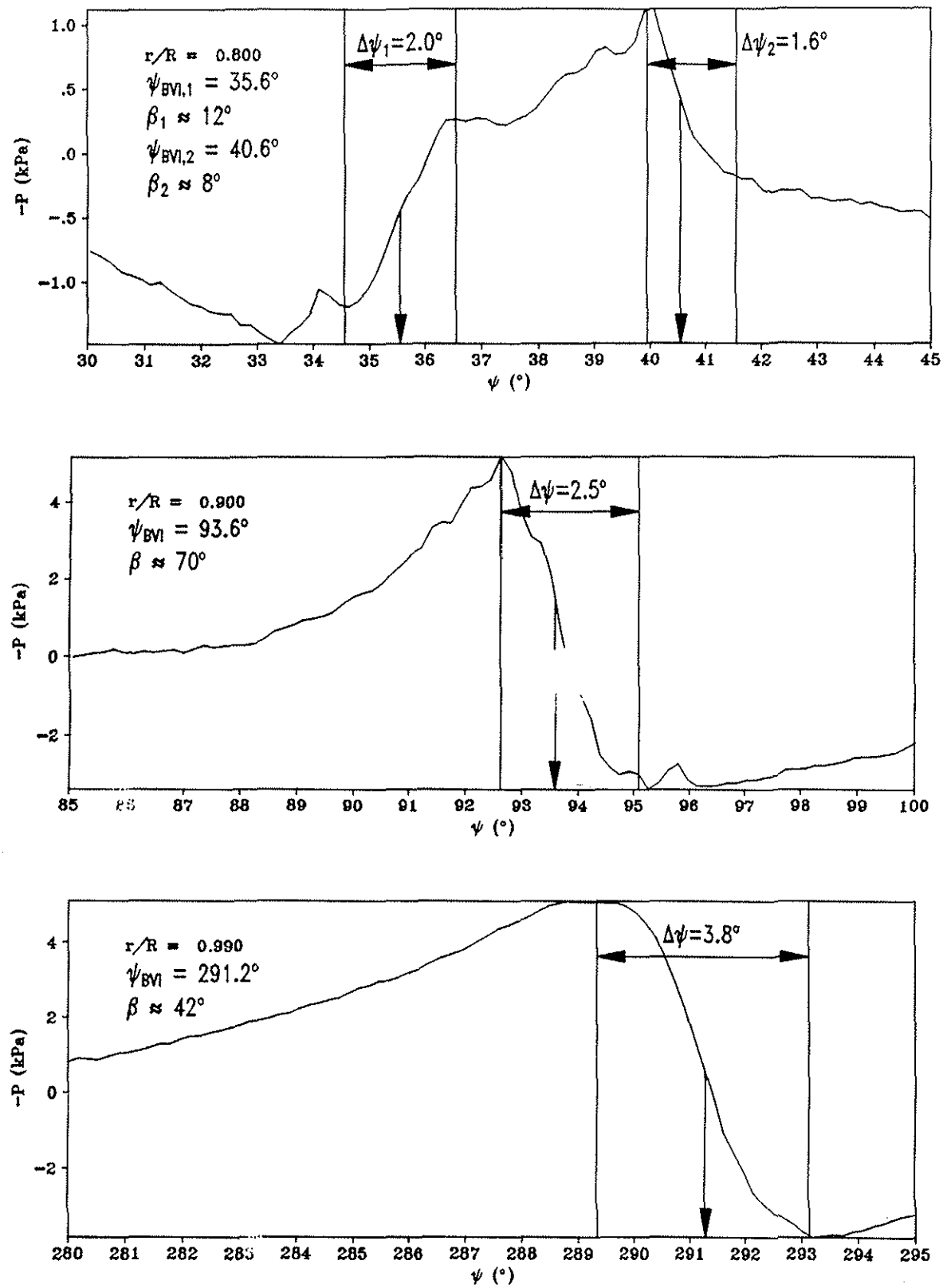


Figure 10: Leading edge pressure time history at selected locations for vortex core radius evaluation. Sensor position: 3% chord, upper side. $\mu = 0.314$, $\alpha_S = -0.9°$, $C_T/\sigma = 0.058$.

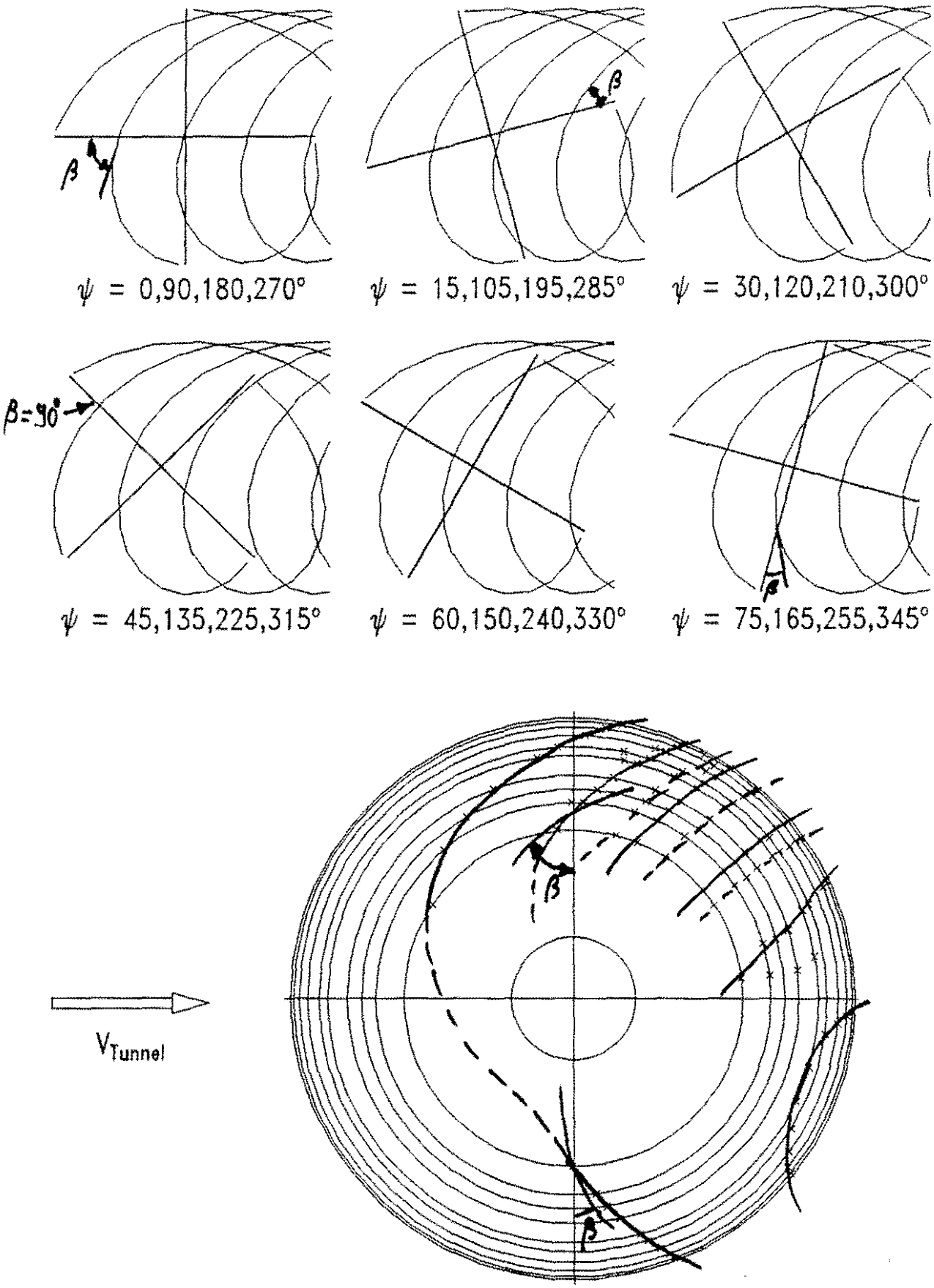


Figure 11: Wake geometry and instantaneous vortex positions at various BVI locations for identification of the angle $\beta$. $\mu = 0.314$, $\alpha_S = -0.9°$, $C_T/\sigma = 0.058$.

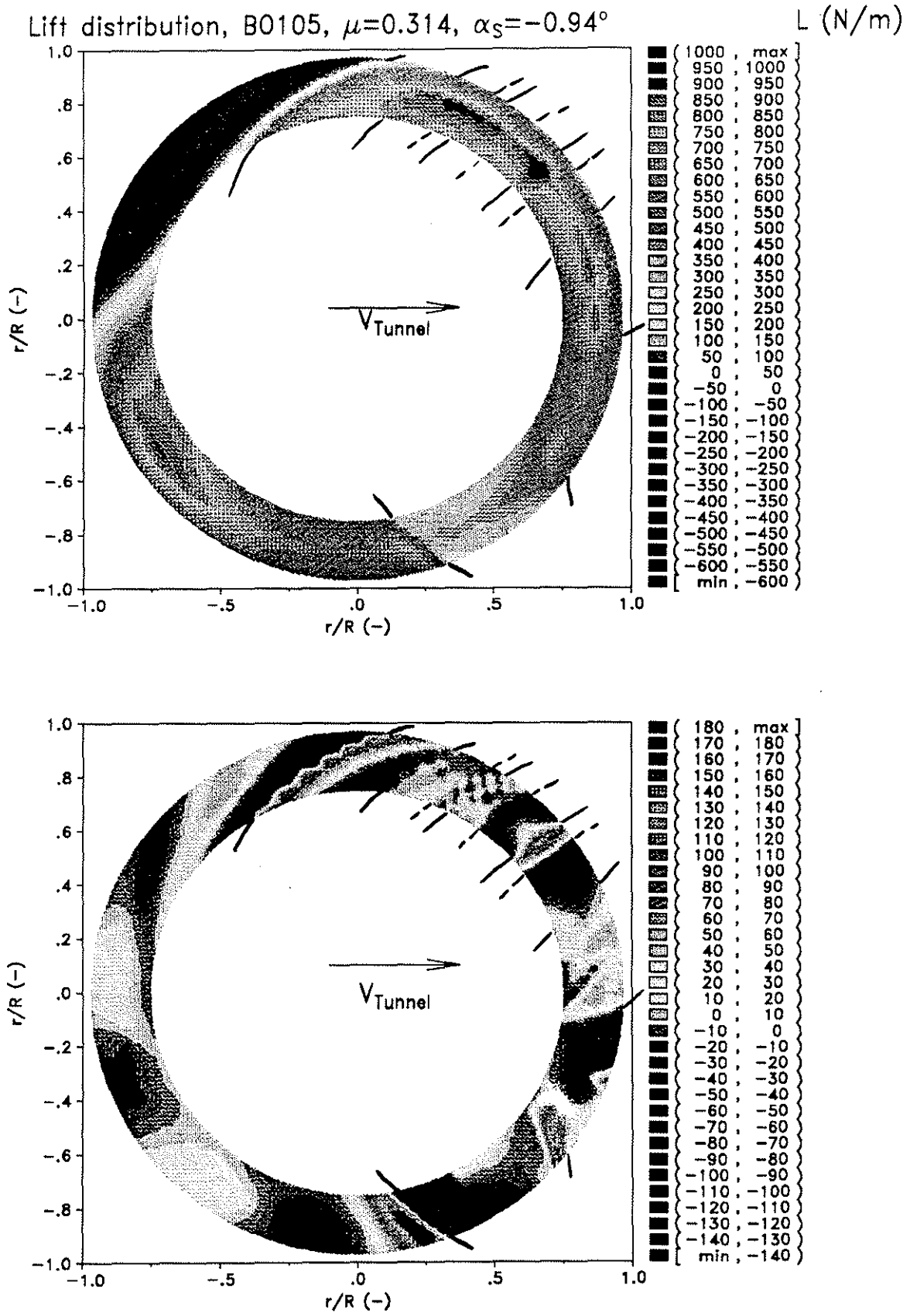


Figure 12: Aerodynamic lift distribution, unfiltered (top) and the first 6 harmonics subtracted (below). $\mu = 0.314$, $\alpha_S = -0.9°$, $C_T/\sigma = 0.058$.

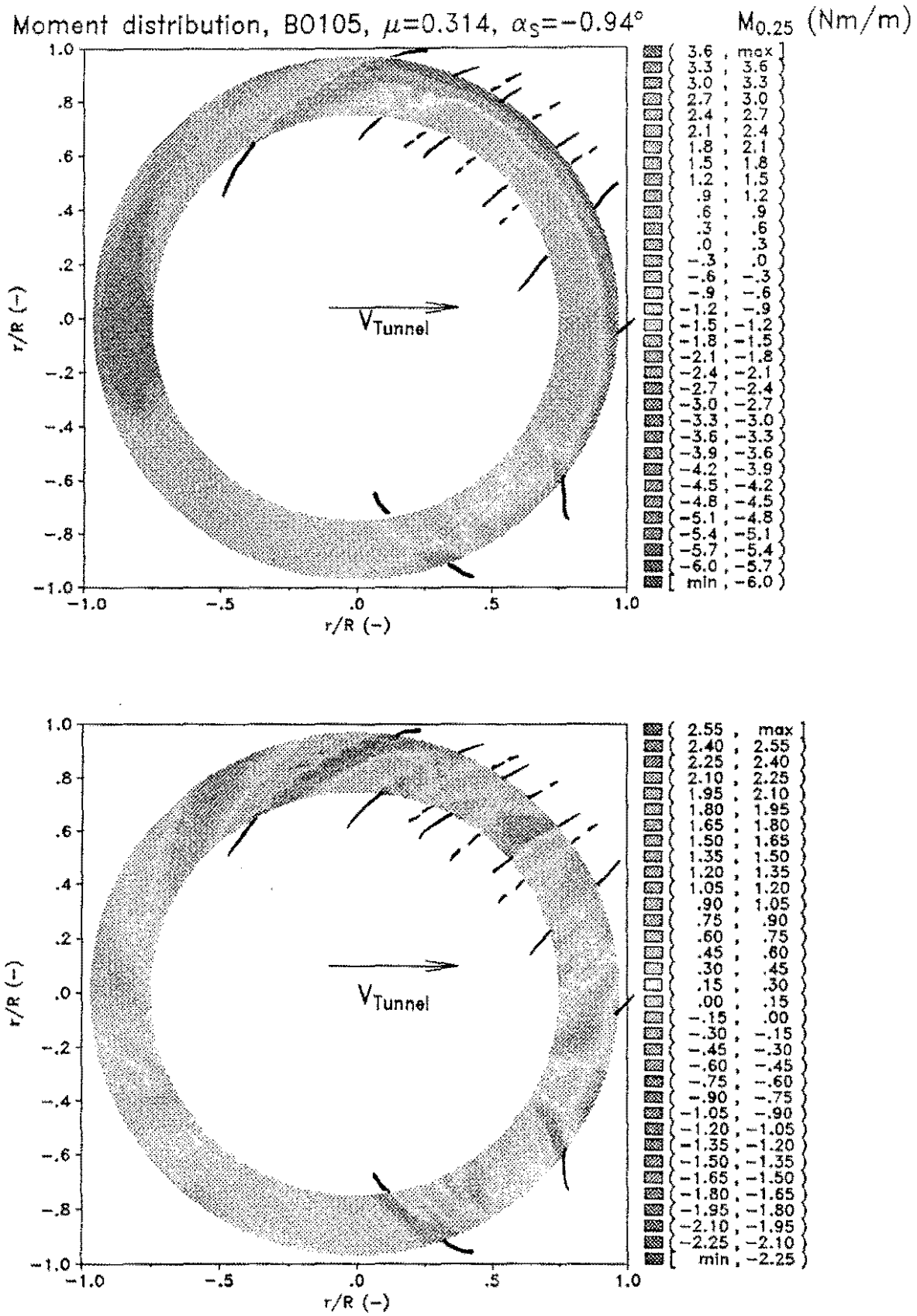


Figure 13: Aerodynamic moment distribution about $c/4$, unfiltered (top) and the first 10 harmonics subtracted (below). $\mu = 0.314$, $\alpha_S = -0.9°$, $C_T/\sigma = 0.058$.